Ceramics International 50 (2024) 22936–22946

Contents lists available at ScienceDirect

Ceramics International

journal homepage: www.elsevier.com/locate/ceramint

$Sr_6Y(PO_4)_5$: Nd^{3+} a novel whitlockite-type phosphor for optical temperature sensing applications: Synthesis and luminescence properties

Ines Mokni [a], Sami Slimi [b], Abdessalem Badri [c], Rosa Maria Solé [b], Magdalena Aguiló [b], Francesc Díaz [b], Brahim Ayed [a], Xavier Mateos [b,*,1]

[a] Laboratory of Physico-chemistry of Materials (LR01ES19), Faculty of Sciences, University of Monastir, Tunisia
[b] Universitat Rovira i Virgili, URV, Física i Cristal·lografia de Materials, (FiCMA), Marcel·lí Domingo 1, 43007, Tarragona, Spain
[c] Laboratory of Interfacial and Advanced Materials (LR11ES55), Faculty of Sciences, University of Monastir, 5000, Monastir, Tunisia

ARTICLE INFO

Handling Editor: Dr P. Vincenzini

Keywords:
Whitlockite-type phosphate
Near infrared excitation
Trivalent neodymium ions
Optical thermometry
Biological application

ABSTRACT

Active research in science and technology is improving the development of materials that emit infrared light, with the aim of better optical thermometric sensors. In this paper we report the synthesis of a new NIR-emitting phosphate phosphor, $Sr_6Y(PO_4)_5$:Nd^{3+} (SYP: Nd^{3+}), at differing concentrations of Nd^{3+} using a conventional solid-state reaction route. X-ray diffraction analysis showed that the prepared phosphors exhibit a singular phase with a monoclinic whitlockite structure (space group *I2/a*). SEM images show micrometer-sized particle. FTIR and Raman spectroscopies confirm the presence of PO_4^{3-} groups in the examined phosphates. Luminescence features, comprising emission spectra, concentration quenching, and fluorescence lifetime, were investigated for the prepared SYP: Nd^{3+} samples at various Nd^{3+} doping concentrations. Excited at 808 nm, the phosphors emitted near-infrared light with four distinct bands corresponding to specific Nd^{3+} transitions from $^4F_{3/2}$ to ($^4I_{9/2}$, $^4I_{11/2}$ and $^4I_{13/2}$) and $^4F_{5/2}$ to $^4I_{11/2}$, falling within the first and second biological windows (NIR-I and NIR-II). Importantly, Nd^{3+} emission characteristics are affected by concentration and temperature. The powders' effectiveness as optical temperature sensors using fluorescence intensity ratio (FIR) between coupled and non-coupled levels was researched across 303–473 K, resulting in two distinctive FIR-based temperature sensor strategies employing emissions at 874.8 nm ($^4F^{3/2} \rightarrow {}^4I_{9/2}$) and 956 nm ($^4F_{5/2} \rightarrow {}^4I_{11/2}$) transitions, all within the first biological window for excitation and emission. Using this method, SYP: Nd^{3+} revealed a notably elevated sensitivity of approximately 1.16 $\%K^{-1}$ at 303 K, surpassing other Nd^{3+}-doped materials when stimulated within the infrared range. These results strongly suggest the prospective applicability of the analyzed material in monitoring the temperature of biological systems.

1. Introduction

Recently, significant research efforts have been invested to advancing the creation of light-emitting substances known as phosphors. Phosphors have diverse applications spanning fields like optics [1,2], electronics [3], catalysis [4] and laser engineering [5]. Crucially, selecting the right host material and dopant ion (among the rare earth elements) stands as a pivotal step in creating high-performance phosphor materials. Inorganic phosphates are excellent hosts for optically active rare earth (RE) ions due to several advantages [6–10]. These include the ability for low-temperature synthesis, strong stability against heat and chemicals, relatively broadband gaps, low toxicity and moderate phonon energies. Moreover, their multiple non-equivalent cationic sites with varying ionic radii and coordination spheres allow for a diverse range of potential cation substitutions. By merging phosphates with rare earth elements results in materials exhibiting significant luminescent characteristics. These materials have attracted significant interest due to their usefulness in various fields such as optical communication, solid-state lasers, solar cell technology (as wavelength converters), multicolor displays, optical temperature sensing (luminescent thermometers) and bioimaging [11–15]. These varied uses result from the distinct characteristics acquired by adding rare earth elements to the material.

Temperature is a primary parameter across scientific disciplines and

* Corresponding author.
E-mail address: xavier.mateos@urv.cat (X. Mateos).
[1] Serra Húnter Fellow

https://doi.org/10.1016/j.ceramint.2024.04.018
Received 3 February 2024; Received in revised form 21 March 2024; Accepted 1 April 2024
Available online 2 April 2024

finds extensive use in everyday sensor applications. Temperature sensors currently dominate around 80 % of the market and are expected to reach an estimated value of $8.8 billion by 2027 (Grand View Research, Inc [16,17]). Temperature can be measured using via contact or non-contact methods. While traditional contact thermometers lack the precision needed for sub-micron temperature measurements, industries such as biomedicine require advanced non-contact thermal sensor technologies to satisfy their stringent requirements [18,19].

Different aspects of phosphor materials, such as their luminescence decay time [20], peak position [21], luminescence intensity [22], luminescence color [23], and emission bandwidth [24], can be affected by temperature changes. As a result, measuring temperature through luminescence involves various methods, such as comparing the fluorescence intensity ratio (FIR), examining lifetime duration, observation of the shifts in the emitted light, assessing polarization, and analyzing emitted light width.

Within these methods, self-referencing ratiometric luminescence thermometer, known as the fluorescence intensity ratio (FIR) technique, has gained considerable attention due to its robust luminescence and exceptional sensitivity to temperature changes. It offers a various advantage over alternative methods and has effectively addresses their technical limitations by observing the temperature-induced changes in the energy levels of two emissions (E1 and E2) from either single or dual luminescent centers. This approach aims to decrease reliance on measurement conditions such as spectrum loss, fluctuations in pumping intensity, and issues related to electromagnetic compatibility [25,26]. In order to ascertain the temperature measurement capacity and efficiency of thermometers, it is essential to consider factors such as absolute sensitivity (*Sa*), relative sensitivity (*Sr*), temporal resolution and measurement consistency in terms of repeatability and reproducibility [27].

To improve temperature measurements over a broad spectrum, scientists have incorporated various RE elements in phosphate host materials. These elements encompass Praseodymium (Pr^{3+}), Neodymium (Nd^{3+}), Samarium (Sm^{3+}), Europium (Eu^{3+}), Terbium (Tb^{3+}), Holmium (Ho^{3+}), Erbium (Er^{3+}), and Thulium (Tm^{3+}). Particularly, Nd^{3+} ions within phosphates have garnered significant attention for their photoluminescent properties, extensively researched due to their intricate energy level configuration. Nd^{3+} ions demonstrate versatility in being stimulated and emitting light across ultraviolet, visible, and infrared wavelengths, showcasing numerous closely linked energy levels. Various excitation routes in materials containing singly, doubly, or triply doped Nd^{3+} ions encompass processes such as upconversion, downconversion, temperature-sensitive absorption capability, cross-relaxation, excited-state absorption, and the thermal coupling of energy levels [28,29].

Phosphate materials containing Nd^{3+} as a dopant react to near-infrared radiation at 808 nm, resulting in an effective emission of light in the near-infrared (NIR) region. This emission arises from transitions between energy levels, namely the $^4F_{3/2}$ and ^4I_J (J = 9/2, 11/2, and 13/2). These emissions occur in the biological transparency windows, specifically the first (700–950 nm) and second (1000–1350 nm) ranges. This characteristic makes Nd^{3+} doped phosphate materials a compelling choice for potential applications in medicine and biology [30]. Nd^{3+} is commonly used in luminescence thermometry due to its closely positioned energy levels and emissions in the near-infrared spectrum. Its energy differences between the levels and Stark sublevels offer improved and more efficient approaches to thermometry, particularly between levels $^4F_{3/2}$ and $^4F_{5/2}$ (TCL1), $^4F_{7/2}$ and $^4F_{3/2}$ (TCL2), and $^4F_{7/2}$ and $^4F_{5/2}$ (TCL3). This enables heightened sensitivity within the critical physiological temperature range (293–333 K), which is essential for many biological processes [31,32].

Accordingly, the present study focuses on the production and investigation of a new phosphor material, $Sr_6Y(PO_4)_5$, incorporating Nd^{3+} as a dopant. The research thoroughly scrutinized its structure, luminescent, and thermometric characteristics, aiming to offer an in-depth understanding of the compound's properties through detailed findings.

2. Experimental

2.1. Synthesis

A series of $Sr_6Y_{(1-x)}(PO_4)_5$: xNd^{3+} (x= 0, 1 %, 2 %, 4 %, 6 %, 8 %, 10 %, 12 %) samples, denoted as SYP:Nd^{3+} were synthesized by solid-state reaction at high temperature. The precursors employed were $SrCO_3$ (Fluka chemika, purity: 98 %), Y_2O_3 (Fluka chemika, purity: 99.98 %), $(NH_4)_2HPO_4$ (Merck, purity: 99 %), Nd_2O_3 (Loba Chemie, purity: 99 %). Stoichiometric amounts of the starting materials were carefully weighed, homogeneously mixed and grounded in an agate mortar by adding a few drops of ethanol. The obtained mixtures were then placed in a platinum crucible and heated in a furnace at a temperature in the range of 673–873 K for 12 h. The obtained products were finally grounded and treated in a final annealing at 1423 K for 24 h.

2.2. Structural and optical characterization

XRD patterns were obtained using a Philips X'Pert automatic diffractometer with Ni filtered Cu-K_α radiation (λ = 1.5406 Å). The elemental composition and morphology were analyzed by scanning electron microscopy (SEM, S-4800, Hitachi) coupled with an energy dispersive X-ray spectrometer (EDX). The IR spectrum was recorded in the range of 400–1800 cm^{-1} using a PerkinElmer Paragon 1000 PC Fourier spectrometer. Raman spectra were measured using a Renishaw InVia confocal Raman microscope equipped with an edge filter, a 50 × objective (Leica), and an Ar^+ ion laser as the excitation source (λ_{exc} = 514 nm). UV–visible diffuse reflectance measurements were performed using a CARY 5000 spectrophotometer (Varian) at room temperature in the range of 200–900 nm using $BaSO_4$ powder as a reference (reflectance of 100 %). The luminescence measurements were conducted using a homemade set-up containing an optical spectrum analyzer (OSA) (350–1200 nm and 1200–2400 nm) coupled to a detector and equipped with a laser diode emitting around 808 nm, a power controller, an oscilloscope and a chopper. An in-house configured set-up was used to measure the temperature-related emission spectra of the sample of interest across the temperature range of 303–473 K.

2.3. Fluorescence intensity ratio temperature sensing method

Monitoring temperature via optical emission from solid-state materials is challenging due to the dependence on radiative and nonradiative transitions between energy levels, making it unreliable with a single transition due to potential signal interference from excitation power or collection system changes. To overcome associated challenges in luminescence thermometer, the Fluorescence Intensity Ratio (FIR) technique has emerged as the primary method to address them and is considered an effective way to enhance temperature precision while simplifying experimental setups. This technique utilizes the monitoring of two emission bands from distinct energy levels (E1 and E2) with varying temperature dependencies. Here, one emission band will act as a point of reference for the other, and alterations in the intensity ratio between these bands will signal a change in temperature [26].

If the energy separation surpasses ~2000 cm^{-1} between these levels, they are termed as non-thermally coupled levels (non-TCLs). Nonetheless, the FIR between these levels may still show a reliance on temperature due to interlinked populations influenced by temperature-dependent transition mechanisms like cross relaxations (CR) and phonon-assisted energy transfers (ET). Conversely, when the energy difference between the most energetic (E2) and least energetic (E1) emitter levels is below ~2000 cm^{-1}, thermal energy enables electronic transitions between these levels. Consequently, these levels will be referred to as thermally coupled levels (TCLs), and their population distribution can be described using the Boltzmann distribution (1) [30,

33]:

$$FIR = \frac{I_2}{I_1} = B \times exp\left(-\frac{\Delta E}{kT}\right), B = \frac{g_2\,\sigma_{2j} w_{2j}}{g_1 \sigma_{1j} w_{1j}} \quad (1)$$

Here, I_1 and I_2 represent the emission intensity from the higher and the lower-energy excited state respectively. k is Boltzmann's constant, ΔE denotes the energy variance between the thermalized excited states while B stands for an experimental constant incorporating the level's degeneracy ($2J + 1$), emission cross section (σ_i), and angular frequency of the transition between the involved levels (ω_i).

Evaluating the performance of thermometer materials relies significantly on sensitivity, which can be categorized into absolute and relative types. Absolute sensitivity is defined as the change in *FIR* when the temperature shifts by 1 K (K), measured in units of K^{-1}, and can be computed using:

$$Sa = FIR \times \frac{\Delta E}{k} \times \frac{1}{T^2}\ \left(K^{-1}\right) \quad (2)$$

The relative sensitivity signifies the percentage of the *FIR* change concerning itself when the temperature shifts by 1 K, indicated in $\%K^{-1}$. The calculation is given by:

$$Sr = \frac{1}{FIR} \times \frac{\delta FIR}{\delta T} \times 100\% = \frac{\Delta E}{kT^2} \times 100\ \left(\%K^{-1}\right) \quad (3)$$

Within this approach, *Sr* stands out as the paramount comparative parameter among sensors of similar types or those employing diverse methodologies. It solely relies on temperature and the energy gap between excited levels, specifically when utilizing a set of thermally coupled levels without substantial overlap between their emission bands.

In addition, by utilizing the thermal coupling among Stark sub-levels in rare earth doped solids, FIR temperature sensors can be developed, particularly in Nd-doped systems targeting optical sensing within the biological window, typically employing transitions from the $^4F_{3/2}$ Stark sublevels. In certain cases, these sublevels' ratio behaves like an isolated two-level system (relatively unaffected by higher-energy levels ($^4F_{5/2}$ and $^4F_{7/2}$), following the Boltzmann distribution (Eq. (1)) [34].

Understanding a thermometer's performance involves studying its uncertainty, reproducibility, and how experimental conditions affect its readings [33]. Among these elements, the temperature uncertainty (or resolution, δT) is particularly significant as it determines the smallest temperature variation that can be identified in practical operational settings:

$$\delta T = \frac{\Delta FIR}{FIR} \times \frac{1}{Sr} \quad (4)$$

Sr has been defined previously and $\Delta FIR/FIR$ stands for the relative uncertainty in the temperature measurement parameter during the measurement process.

Additionally, the significance of temperature cycling in thermometer readout repeatability lies in the ability to assess the stability and reliability of the thermometer under varying thermal conditions. This evaluation is measured using a specific mathematical expression:

$$R = \left[1 - \frac{max(|\Delta_c - \Delta_i|)}{\Delta_c}\right] \quad (5)$$

Herein, the average temperature measurement parameter is represented by Δc, and each measurement value of the temperature measurement parameter is denoted as Δi. Usually, performing 10 successive measurements yields a stable calculation outcome. FIR thermometers using inorganic luminescent materials exhibit remarkable thermal stability, resulting in a high repeatability (R) value.

3. Results and discussion

3.1. Structural characterization

Fig. 1 (a) shows the unit cell of the $Sr_6Y(PO_4)_5$ whitlockite structure where the Y ions are located in an octahedral environment. Adopting the whitlockite structure of β-$Ca_3(PO_4)_2$ with a space group *I2/a* (N°15) [35]. The $Sr_6Y(PO_4)_5$ lattice constants were obtained from Rietveld refinement based on the XRD data as outlined in Fig. 1 (b) with the aid of the WinPLOTR/Fullprof program [36], of as follows: a = 17.9917 (2) Å, b = 10.6745 (1) Å, c = 18.4679 (2) Å, β = 132.8913 (3) °, V = 2598 (1) $Å^3$ and Z = 4. The resulting reliability factors (Rp = 10.3, Rwp = 13.9 and $\chi 2$ = 4.33) reflect a good match between the diffraction patterns observed experimentally and those calculated. An YO_6 octahedron is located at the position centered of the monoclinic cell, but all other YO_6 octahedra are positioned at the corners and edges of the monoclinic cell. In addition, SrO_8 polyhedra and PO_4 tetrahedra are distributed in the monoclinic cell, where the P (1)O_4 tetrahedra are oriented in an ordered manner. However, the other P and O atoms of the phosphate ions are not on the triple axis of rotation.

Additionally, the permissible percentage difference (R_a) between the ionic radiation of the substituted ion (Rs) and that of the doped ion (R_d) must not exceed 30% [37] and is calculated using the following formula (6) [38]:

$$\%R_a = \left(\frac{R_s - R_d}{R_s}\right) \times 100 \quad (6)$$

It is noteworthy that the ionic radius of Nd^{3+} ions with a CN of 6 is measured at 1.123 Å, while Y^{3+} ions, also possessing a CN of 6, exhibit an ionic radius of 1.040 Å [39]. Consequently, the R_a between Y^{3+} and Nd^{3+} is calculated to be 7.98 %, a value significantly below the threshold of 30 %. This substantial difference indicates that Nd^{3+} ions effectively substitute Y^{3+} ions in the crystal lattice, resulting in the formation of $Sr_6Y_{1-x}Nd_x(PO_4)_5$ (where x represents the doping concentration of Nd^{3+} ions). The successful substitution is attributed to the same charge and comparable ionic radii between Nd^{3+} and Y^{3+}.

XRD analysis was used to determine the phase purity of the $Sr_6Y(PO_4)_5$:xNd^{3+} phosphors (x = 0.01, 0.06, 0.12). The results are illustrated in Fig. 2 (a). The diffraction patterns of the samples matched the standard card (ICSD-59722) for $Sr_9In(PO_4)_7$, indicating that the presence of Nd^{3+} dopant up to a concentration of 12 mol% did not result in any impurity phases. Fig. 2 (b) is a partial XRD magnification of the samples at 2θ = 29–31°. With the increase of Nd^{3+} content, the main peak slightly deviates towards a small angle. Bragg's diffraction formula ($2d\sin\theta = n\lambda$) can explain the occurrence of this phenomenon because the radius of Nd^{3+} (1.123 Å) is greater than that of Y^{3+} (1.040 Å), the d in the formula increases, causing θ to decrease.

Crystallite size (Dc) of SYP and SYP: Nd^{3+} materials significantly influence their physical and optical characteristics, and it can be determined using the Scherrer formula (7) [40], which calculates the crystallite size (Dc):

$$D_c = \frac{K\lambda}{\beta \cos\theta} \quad (7)$$

The crystallite size (Dc), measured in nanometers (nm), λ the wavelength of X-rays employed (typically denoted by λ = 1.540564 Å for monochromatic Cu-K_α radiation), θ the diffraction angle, a form factor (K, approximately 0.89), and the width at half maximum (β) expressed in radians. The determined crystallite sizes, based on diffraction angles of 29.838°, 29.837°, 29.675°, and 29.480° for the compositions $Sr_6Y(PO_4)_5$, $Sr_6Y_{0.99}(PO_4)_5$:0.01 Nd^{3+}, $Sr_6Y_{0.94}(PO_4)_5$:0.06 Nd^{3+} and $Sr_6Y_{0.88}(PO_4)_5$:0.12 Nd^{3+}, respectively, showed an upward trend with higher Nd^{3+} concentration: 50.6080 nm, 60.2640 nm, 63.0816 nm and 64.7794 nm, respectively.

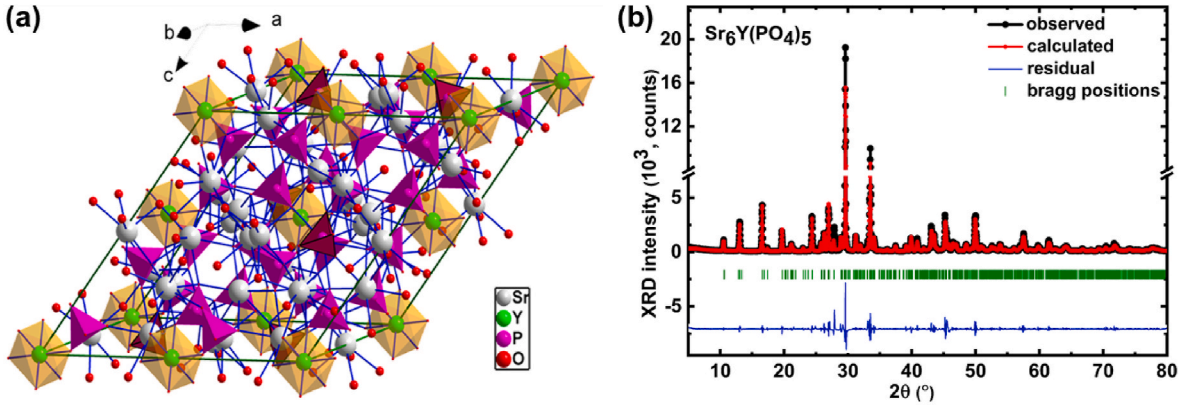

Fig. 1. **(a)** The unit-cell structure of $Sr_6Y(PO_4)_5$. **(b)** Rietveld refinement of X-ray powder diffraction of $Sr_6Y(PO_4)_5$.

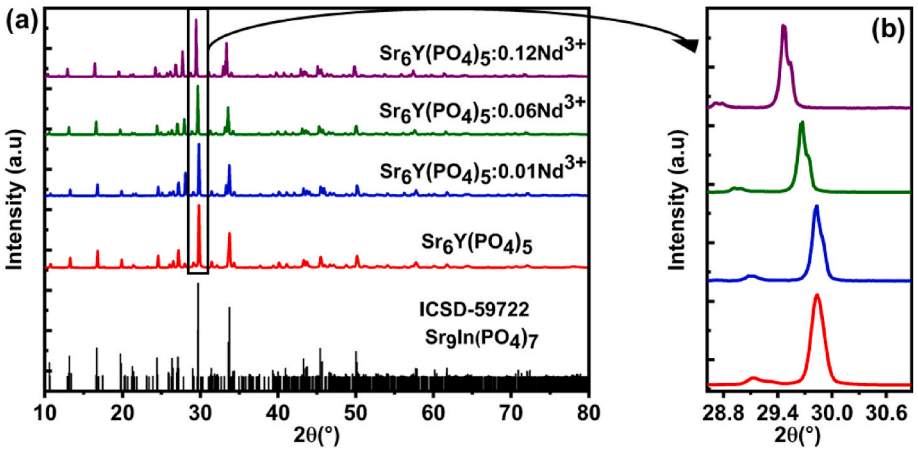

Fig. 2. **(a)** Comparative X-ray powder diffraction (XRD) patterns of $Sr_6Y(PO_4)_5$ and Nd^{3+} doped-$Sr_6Y(PO_4)_5$ samples. **(b)** Enlarged XRD view of the peak with the strongest intensity.

3.2. SEM and EDX

Fig. 3 reports the SEM-EDX results for samples $Sr_6Y(PO_4)_5$ and $Sr_6Y_{0.88}(PO4)_5$:0.12 Nd^{3+}. The texture consists of spherical agglomerated particles with an average size in the micrometer range (Fig. 3 (a)). In addition, the EDX spectra shown in Fig. 3(b–c) revealed the presence of the chemical elements (Sr, Y, Nd, P and O) with atomic percentages consistent with those theoretically calculated from the chemical formulas of the samples. Furthermore, the EDX maps of the powders shown in Fig. 3 (d) confirm the homogeneous distribution of all the previously mentioned elements in the area of interest of the $Sr_6Y_{0.88}(PO_4)_5$: 0,12 Nd^{3+} sample.

3.3. Fourier-transform infrared (FTIR) and Raman spectroscopies

To prove the presence of PO_4^{3-} groups and highlight their vibrational modes, the SYP crystal was analyzed by IR spectroscopy. The infrared spectrum obtained is shown in Fig. 4 (a). The observed bands were attributed to the vibrational modes of the phosphate groups by comparison with previous work on monophosphates [41–43]. The bands observed between 1128 and 1026 cm^{-1} correspond to the triply degenerate antisymmetric *P–O* stretching mode (ν_3). The two intense bands located at 979 cm^{-1} and 928 cm^{-1} are attributed to symmetrical *P–O* stretching (ν_1). The triply degenerate antisymmetric *O–P–O* bending mode (ν_4) was observed around 615, 595,581 and 539 cm^{-1}. The bands observed at 469 and 421 cm^{-1} corresponds to the doubly degenerate symmetrical *O–P–O* bending mode (ν_2).

Fig. 4 (b) shows the Raman spectra of $Sr_6Y(PO_4)_5$ and $Sr_6Y_{1-x}(PO_4)_5$: xNd^{3+} (x = 0.01, 0.06, 0.12). The bands have been assigned in accordance with previous studies [43–48]. Pics appearing amongst 962 cm^{-1} and 1083 cm^{-1} correspond to stretching vibrations in PO_4^{3-} tetrahedra. Pics between 414 and 624 cm^{-1} correspond to bending modes of the phosphate anion. Table 1 summarizes the FTIR-Raman band assignments.

3.4. UV–vis diffuse-reflectance analysis

UV–vis diffuse reflectance spectra (DRS) measured in the 200–900 nm wavelength range for $Sr_6Y_{1-x}(PO_4)_5$: xNd^{3+} ($0 \leq x \leq 0.12$) are shown in Fig. 5 (a). The diffuse reflectance patterns of Nd^{3+}-doped $Sr_6Y(PO_4)_5$ reveal pronounced and broad absorption bands across the UV–Visible–NIR regions [49]. The bands observed at 475, 512, 525, 580, 735 and 804 nm are characteristic of Nd^{3+} transitions $^4I_{9/2}\rightarrow(^2K_{15/2} + {}^2G_{9/2})$, $^4I_{9/2} \rightarrow {}^4G_{9/2}$, $^4I_{9/2}\rightarrow (^2K_{13/2} + {}^4G_{7/2})$, $^4I_{9/2}\rightarrow(^4G_{5/2} + {}^2G_{7/2})$, $^4I_{9/2}\rightarrow (^4S_{3/2} + {}^4F_{7/2})$ and $^4I_{9/2}\rightarrow(^4F_{5/2} + {}^2H_{9/2})$ respectively and confirming the doping of the phosphate material $Sr_6Y(PO_4)_5$ with Nd^{3+} ions. Nd^{3+} ions, absorbing around 804 nm, are seen as a strong contender for generating efficient emissions in the I- and II-BWs.

In order to estimate the optical band gap of the host SYP and SYP: Nd^{3+}, the reflectance spectra were converted and the optical band gap Fig. 5 (b) of the samples was calculated via Tauc's relation (8) [50,51]:

$$\boldsymbol{F}(\boldsymbol{R})\boldsymbol{h\nu} = \boldsymbol{A}(\boldsymbol{h\nu} - \boldsymbol{Eg})^{\boldsymbol{n}} \quad (8)$$

Where *A* is absorption coefficient, *R* expresses the reflectivity of the samples, $h\nu$ means the photon energy, E_g denotes the energy band gap,

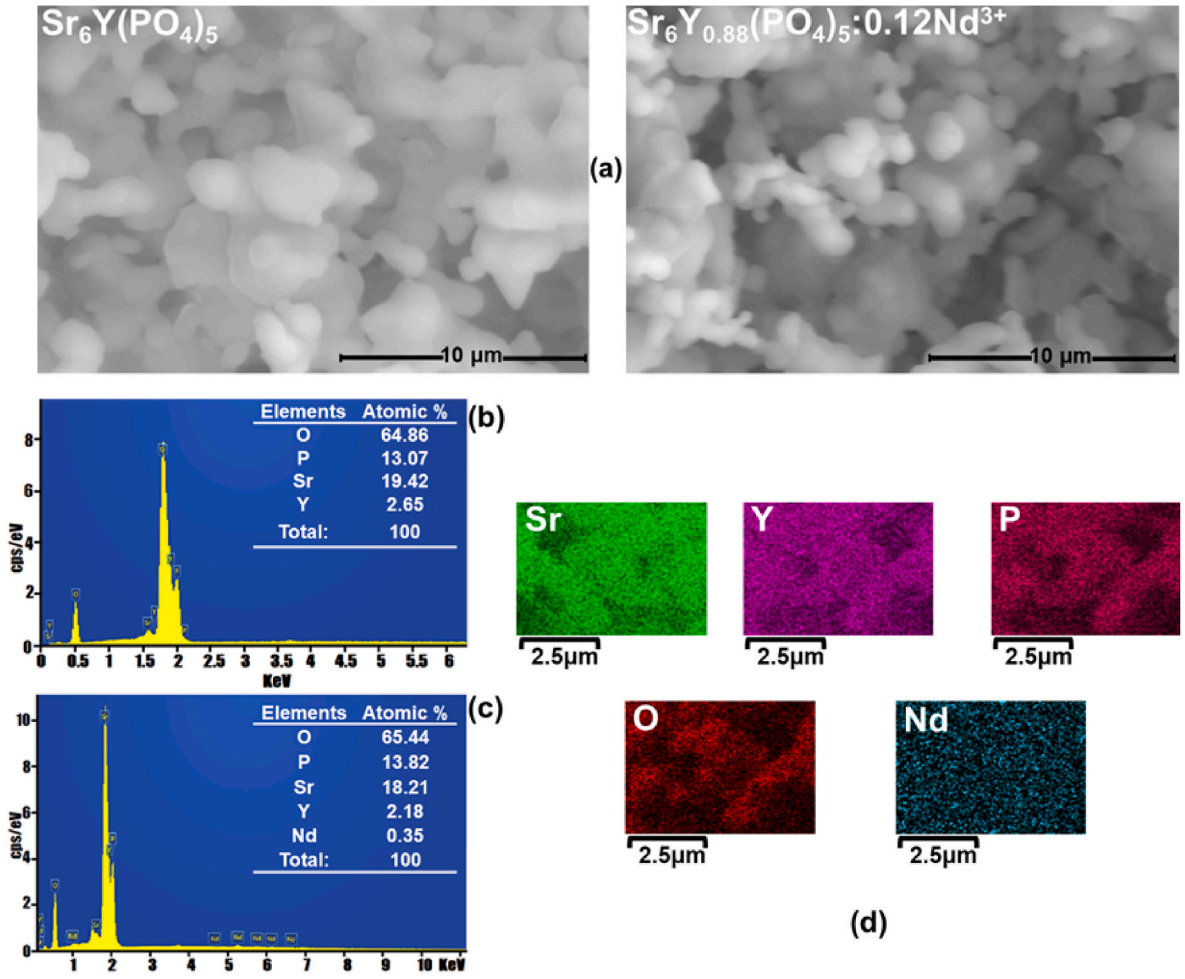

Fig. 3. **(a)** SEM results of $Sr_6Y(PO_4)_5$ and $Sr_6Y_{0.88}(PO_4)_5$:0.12 Nd^{3+} powders. **(b–c)** EDX results of $Sr_6Y(PO_4)_5$ and $Sr_6Y_{0.88}(PO_4)_5$:0.12 Nd^{3+} powders respectively, inset shows the determined chemical composition. **(d)** EDX-based element mapping for the $Sr_6Y_{0.88}(PO4)_5$:0.12 Nd^{3+} powder: (Sr, Y, Nd, P and O).

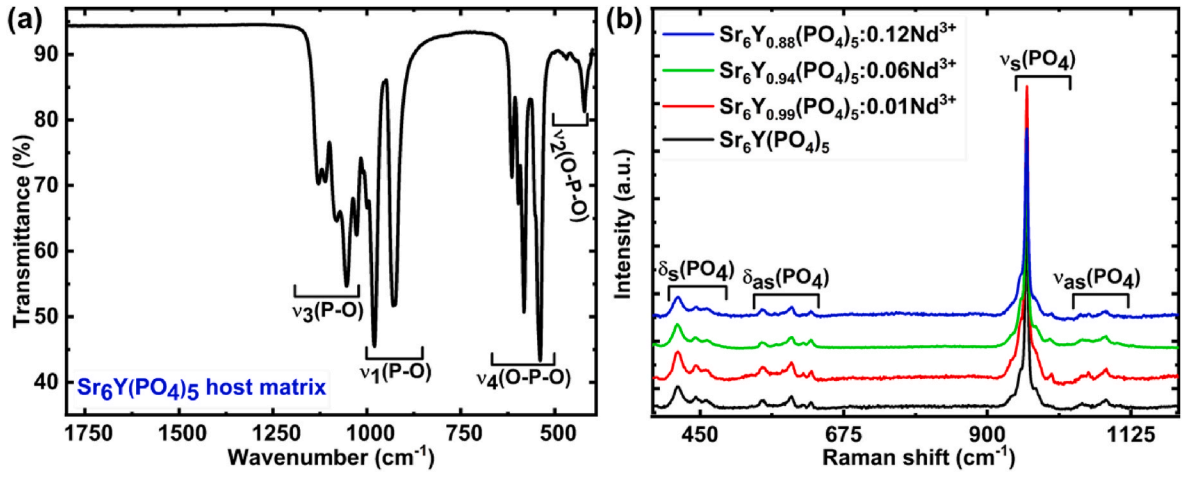

Fig. 4. **(a)** FTIR spectrum of $Sr_6Y(PO_4)_5$ sample. **(b)** Raman spectra of $Sr_6Y(PO_4)_5$ and Nd^{3+} doped-$Sr_6Y(PO_4)_5$ samples.

and *n* is dependent on the nature of transition (n = 1/2, 2, 3, 3/2 for direct, indirect allowed transition and forbidden transition), respectively. Considering only the indirect allowed transitions, the variations in E_g, with dopant Nd^{3+} concentration in the host are shown in Fig. 5 (b).

3.5. Luminescence properties

3.5.1. Emission spectra

To explore the photoluminescence (PL) characteristics, tests were conducted on SYP:xNd^{3+} samples with varying compositions ($0.01 \leq x \leq 0.12$) at room temperature, employing a continuous-wave (CW) laser

Table 1
Assignment of Fourier-transform infrared (FTIR) and Raman bands in SYP:Nd^{3+} phosphors.

FTIR band position (cm^{-1})	Assignment	Raman band position (cm^{-1})	Assignment
1128, 1111, 1080, 1054, 1026	Antisymmetric stretching vibrations	**1083, 1054,1048**	Antisymmetric stretching vibrations of PO_4^{3-} units
615, 595, 581, 539	*O–P–O* antisymmetric bending vibrations	**624, 611, 592, 548**	*O–P–O* antisymmetric bending vibrations
979, 928	Symmetric *P–O* stretching	**999, 962**	Symmetric *P–O* stretching
469, 421	Symmetric *O–P–O* bending mode	**462, 444, 414**	Symmetric *O–P–O* bending mode

at a wavelength of 808 nm for excitation. Fig. 6 (a) displays the near-infrared emission spectra of the as prepared samples. In which it is possible to identify the presence of four characteristic emission peaks of Nd^{3+}-doped materials [52,53]: (1) a broad emission peak and its corresponding Stark sublevels appeared from 851 to 935 nm with a maximum at 874.8 nm, associated with the $^4F_{3/2} \rightarrow {}^4I_{9/2}$ transition, (2) from 1024.0 to 1114.0 nm centered at 1058.0 nm, related to $^4F_{3/2} \rightarrow {}^4I_{11/2}$ transition, (3) emission band with an extremely low intensity exists (between 944.4 and 985.0 nm) with a maximum at 956.0 nm that corresponds to the $^4F_{5/2} \rightarrow {}^4I_{11/2}$ transition and the fourth is from 1288.7 to 1420.0 nm with a maximum at 1330.0 nm, stands for $^4F_{3/2} \rightarrow {}^4I_{13/2}$ transition.

For the SYP: Nd^{3+} phosphor, the excitation and emission wavelengths are situated within the boundaries of the first biological window (NIR-1: 650–950 nm) and the second biological window (NIR-2: 1000–1350 nm). This resemblance strongly indicates that this material holds considerable promise as a flexible option for a range of imaging and medical uses [54–56].

The spectrum bands are assigned to specific transitions based on the Dieke diagram [57]. The emission of Nd^{3+} ions in these systems can be achieved using various excitation wavelengths ranging from approximately 350 nm–900 nm. To elucidate the luminescence mechanism of SYP: Nd^{3+} phosphor in the NIR region upon excitation at 808 nm, a simplified energy level diagram of the Nd^{3+} ions in SYP: Nd^{3+} phosphor is depicted in Fig. 6 (b). When pumped at 808 nm, Nd^{3+} ions in their ground state $^4I_{9/2}$ get excited to the higher-level $^4F_{5/2}$, which promptly undergoes a non-radiative process, transferring the electrons to the $^4F_{3/2}$ metastable state. The energy difference between $^4F_{5/2}$ and $^4F_{3/2}$ states is 1000 cm^{-1}, shown by the zigzag arrow. Consequently, the photoluminescence process results in four radiative emissions. Three at 874.8

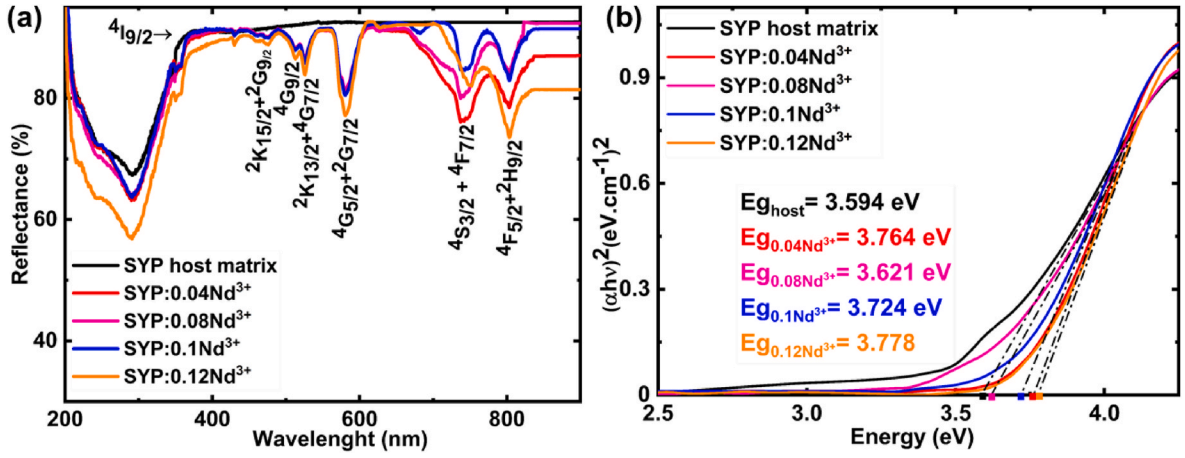

Fig. 5. (a) The diffuse reflection spectra of the $Sr_6Y(PO_4)_5$ and Nd^{3+} doped-$Sr_6Y(PO_4)_5$ samples. **(b)** Tauc's plots of the $Sr_6Y(PO_4)_5$ and Nd^{3+} doped-$Sr_6Y(PO_4)_5$ samples.

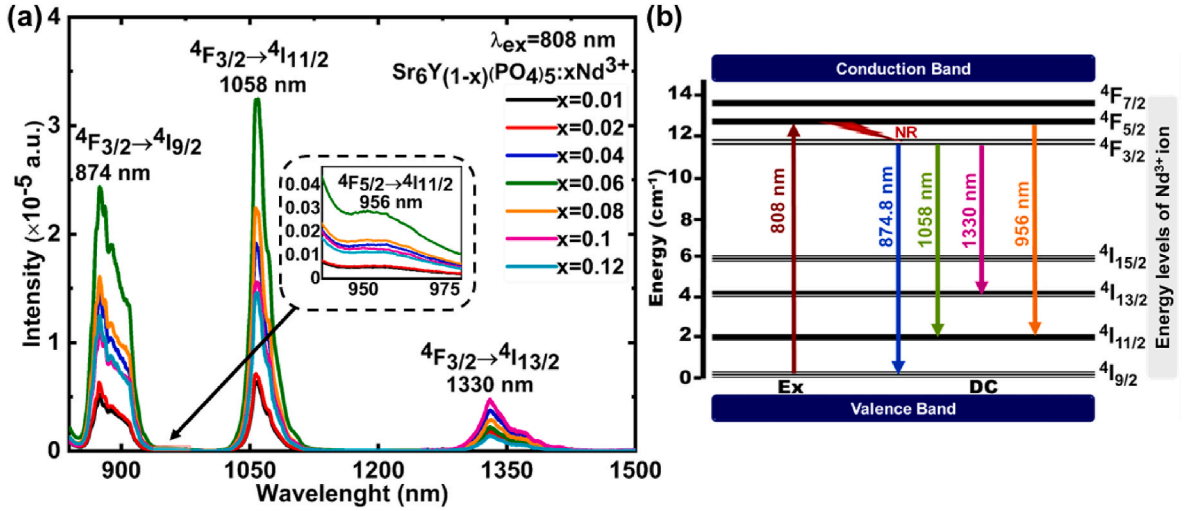

Fig. 6. (a) Emission spectra of $Sr_6Y(PO_4)_5$ doped with x% Nd^{3+} under 808 nm excitation. **(b)** Simplified energy level diagram of Nd^{3+} ion in SYP: Nd^{3+} with mechansims of emissions generation.

nm, 1058 nm, and 1330 nm, which correspond to transitions of Nd^{3+} ions from the $^4F_{3/2}$ level to lower energy levels, namely $^4I_{9/2}$, $^4I_{11/2}$, and $^4I_{13/2}$, respectively. In addition, the fourth radiative emission appeared at 956 nm from $^4F_{5/2}$ to $^4I_{11/2}$ levels.

3.5.2. Concentration quenching and luminescence decay times of Nd^{3+}-doped $Sr_6Y(PO_4)_5$ powders

Fig. 7 (a) shows that when pumped at 808 nm at room temperature, the emission intensities progressively rise with higher concentrations of Nd^{3+} ions, peaking at x = 6 mol%. However, beyond this concentration, the optical intensities of Nd^{3+} ions diminish as their concentration increases. This behavior can be elucidated by the phenomenon known as concentration quenching. The impact of concentration quenching stems from ion-ion interactions, specifically involving the transfer of energy between activator ions such as Nd^{3+} to Nd^{3+}. Identifying the interaction type relies on measuring the critical distance (*Rc*). When *Rc* exceeds 5 Å, it signifies an electric multipolar interaction, while *Rc* below 5 Å indicates exchange interactions. Equation (9) as presented by Blasse [58] enables the calculation of the distance *Rc*:

$$R_c = 2\left[\frac{3V}{4\pi XcN}\right]^{\frac{1}{3}} \tag{9}$$

In which N is the number of cationic sites occupied by activators in one-unit cell, *Xc* is the critical concentration, and V is the volume of the unit cell. The specific values used in our research are as follows: V = 2598 $Å^3$, Xc = 0.06 and N = 4. The calculated value of *Rc* is 27.44 Å, which surpasses the entrance (Rc ≥ 5 Å), indicating that the energy transfer mechanism in SYP: Nd^{3+} appears to follow an electric multipolar interaction.

As per Dexter's theory [59], this form of interaction between neighbour Nd^{3+} ions can be further examined utilizing the provided equation (10):

$$\frac{I}{x} = K\left[1 + \beta(x)^{\frac{\theta}{3}}\right]^{-1} \tag{10}$$

In rearrangement of equation (10):

$$Ln\left(\frac{I}{x}\right) = K' - \left(\frac{\theta}{3} ln\, x\right) \tag{11}$$

Here *I* is the emission intensity, *x* means activator concentration, *K'* represents a constant and *θ* refers to an electric multistage characteristic. When *θ* assume values of 6, 8, and 10, they signify different types of interactions: 6 represents dipole-dipole interactions, 8 refers to dipole-quadrupole interactions, and 10 indicates quadrupole-quadrupole interactions. In Fig. 7 (b), a plot of ln (I/x) versus ln (x) is presented for the emission at 1058 nm, corresponding to the $^4F_{3/2} \rightarrow {}^4I_{11/2}$ transition of SYP: Nd^{3+}. The fitting result for x > 6 mol% shows a linear trend, with a slope of (-θ/3) = −2.021. The value obtained for *θ* is 6.063, with *θ* being approximately 6, suggesting that the mechanism for energy transfer within Nd ions in $Sr_6Y(PO_4)_5$ phosphor happens through dipole-dipole interactions.

The experimental decay patterns (*τexp*) of the $^4F_{3/2} \rightarrow {}^4I_{11/2}$ transition (1058 nm) in $Sr_6Y(PO_4)_5$ powder samples with various concentrations of Nd^{3+} (x = 0.01, 0.02, 0.04, 0.06, 0.08, 0.1, and 0.12 mol) were recorded under 808 nm excitation at room temperature. The decay profiles plotted in Fig. 8 have all been modeled by a single exponential function. As the Nd concentration increases, there is a significant decrease in emission intensities, led to gradually shorter measured luminescence decay times (*τ*): 1.202 ms, 1.126 ms, 0.711 ms, 0.665 ms, 0.632 ms, 0.571 ms, and 0.45 ms for concentrations of x = 0.01, 0.02, 0.04, 0.06, 0.08, 0.1, and 0.12 mol respectively. In fact, the shorter the lifetime with higher doping concentration offers an additional proof of non-radiative energy transfer processes between Nd^{3+} ions in $Sr_6Y(PO_4)_5$.

3.6. Thermometric properties of SYP: Nd^{3+} phosphor

Nd^{3+} is often used in luminescence thermometry because of its closely spaced energy levels and emissions within the near-infrared spectrum [60–62]. Studying the impact of temperature on Nd^{3+} emission bands was also done to explore its sensor capabilities in the selected $Sr_6Y(PO_4)_5$ powder doped with 6 mol% Nd^{3+}. Fig. 9 (a) exemplifies the emission spectra of $Sr_6Y_{0.94}(PO_4)_5$:0.06 Nd^{3+} across a temperature range of 303 K–473 K under a continuous-wave laser excitation centered at 808 nm, revealing diverse behaviors among different bands. When exposed to near-infrared excitation, the luminescent intensities linked to

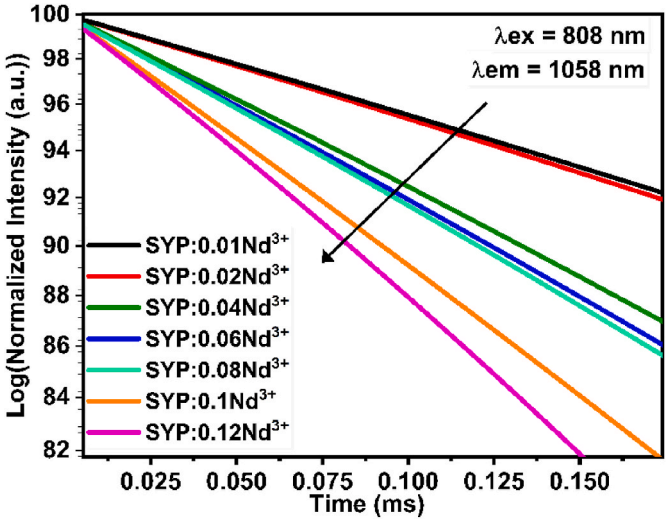

Fig. 8. Photoluminescence decay curves for the $^4F_{3/2} \rightarrow {}^4I_{11/2}$ transition (1058 nm) in SYP: Nd^{3+} tracked under 808 nm excitation.

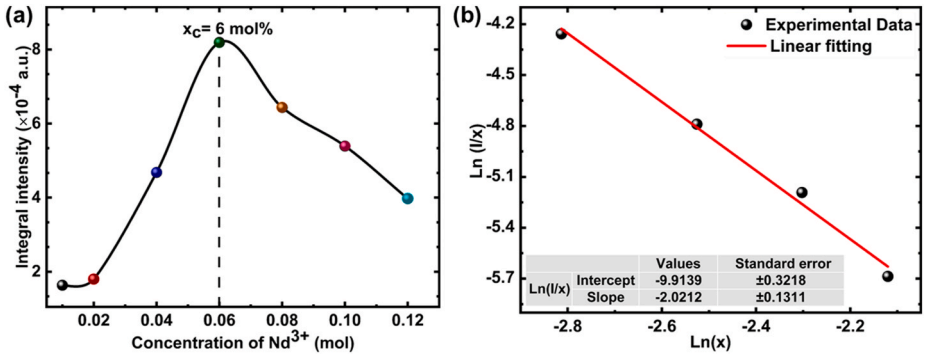

Fig. 7. **(a)** Concentration quenching of Nd^{3+} doped-$Sr_6Y(PO_4)_5$ phosphor. **(b)** Relationship between the ln (I/x) and ln (x) for the $^4F_{3/2} \rightarrow {}^4I_{11/2}$ transitions.

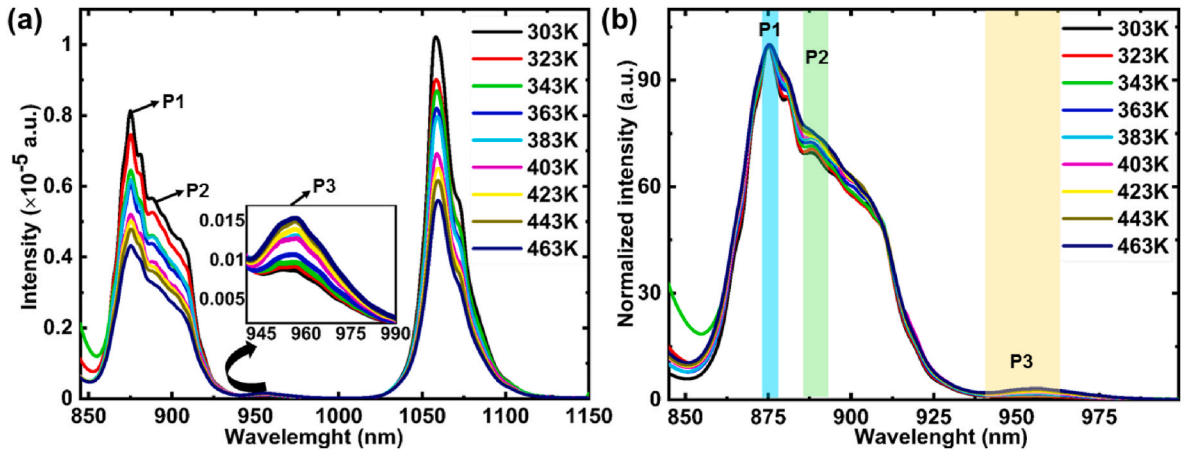

Fig. 9. **(a)** Photoluminescence emission spectra of SYP: Nd^{3+} measured at different temperatures upon 808 nm laser excitation. **(b)** Normalized emission spectra of the $^4F_{3/2}$ to $^4I_{9/2}$ and $^4F_{5/2}$ to $^4I_{11/2}$ transitions.

the $^4F_{5/2} \rightarrow {}^4I_{11/2}$ transition (~956 nm) exhibited an increase with rising environmental temperatures. On the other hand, the intensity of the emission band associated to the $^4F_{3/2}$ to $^4I_{9/2}$ (~874.8 nm) and $^4F_{3/2}$ to $^4I_{11/2}$ (1058 nm) transitions did not exhibit the same trend as the emitted state $^4F_{5/2}$: the emission is reduced when the temperature is increased. This behavior is related with the excitation and emission mechanisms of the Nd^{3+} ions in this phosphate. Such behavior can be elucidated by the fact that Nd^{3+} excitation is a result of a phonon-assisted, one-laser--photon absorption process [63]. Due to thermal coupling among the emitting levels ($^4F_{5/2}$ and $^4F_{3/2}$), a further increase in temperature promotes the increment of more energetic level populations, leading to a decrease in the $^4F_{3/2}$ emission intensity. Nevertheless, under near-infrared excitation, the luminescence intensity from the $^4F_{5/2} \rightarrow {}^4I_{11/2}$ transition increased with temperature elevation.

In pursuit of luminescent thermometry, our focus was directed towards the two specific emission lines of SYP: Nd^{3+}, which occur approximately at 874.8 and 956 nm (Fig. 9 (b)), using the FIR technique to assess temperature sensing applications, section 2.3. Because of the link between higher temperatures and the coupled energy levels, a potential decline in FIR-based sensing capabilities is expected. Nevertheless, this is not alarming due to the usual physiological temperature range of 303–333 K. Our research evaluated sensor efficiency within the broader range of 303–473 K, encompassing the physiological range.

Nd^{3+} has been extensively studied regarding thermal coupling

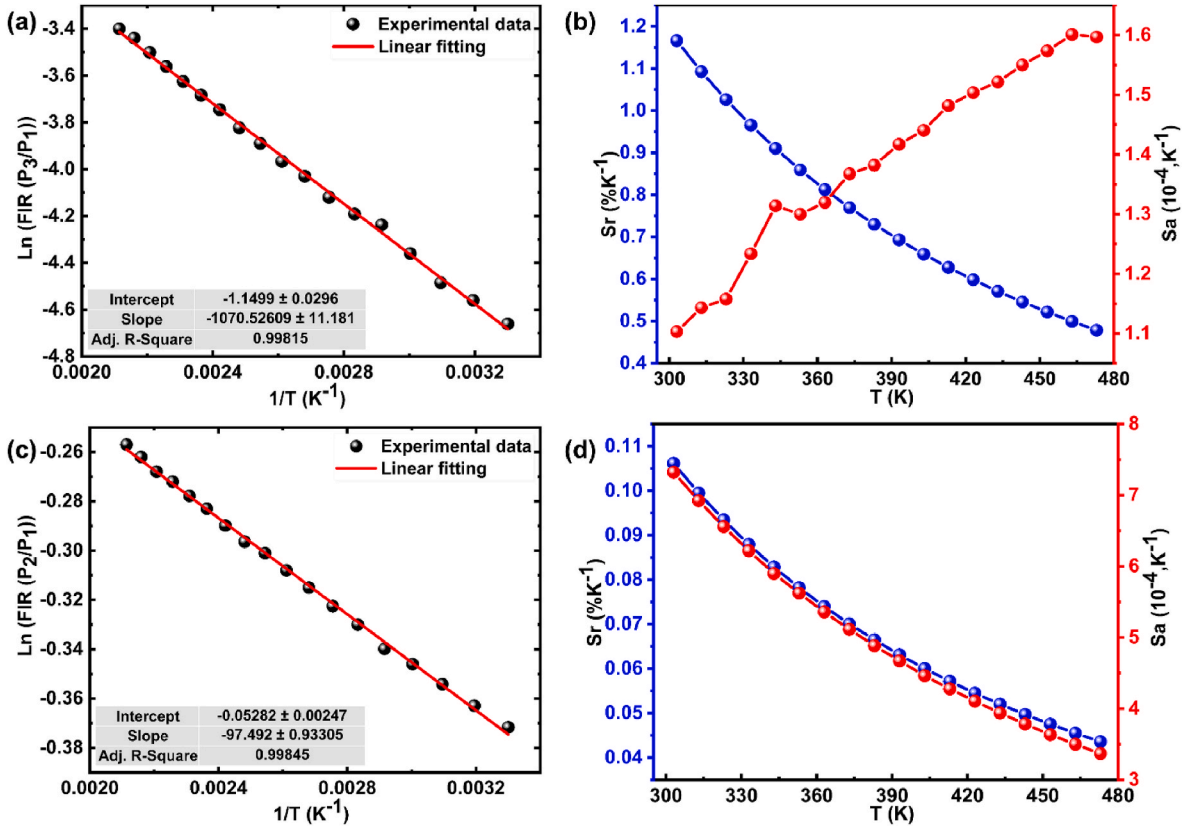

Fig. 10. **(a–c)** Variations in the FIR (P_3/P_1) and FIR (P_2/P_1) signals concerning temperature related to ($^4F_{3/2} \rightarrow {}^4I_{9/2}$ and $^4F_{5/2} \rightarrow {}^4I_{11/2}$) and Stark sublevels ($^4F_{3/2} \rightarrow {}^4I_{9/2}$) transitions, respectively. **(b–d)** Absolute and relative sensitivities calculated for FIR (P_3/P_1) and FIR (P_2/P_1) respectively in $Sr_6Y_{0.94}(PO_4)_5$:0.06 Nd^{3+}.

between its $^4F_{5/2}$ and $^4F_{3/2}$ states for temperature sensing applications. However, the specific transitions $^4F_{3/2} \rightarrow {}^4I_{9/2}$ and $^4F_{5/2} \rightarrow {}^4I_{11/2}$, highlighted as a potential strategy for FIR by André S. Laiaa et al., in 2020 [64], appear to be reported for the first time, drawing our focus and interest. The luminescence spectra of SYP: Nd^{3+} powder under 808 nm excitation and its temperature-dependent changes suggest a promising path for exploring a novel FIR sensing technique termed FIR (P_3/P_1). This approach entails examining intensity variations at 874.8 and 956 nm, which correspond to ($^4F_{3/2} \rightarrow {}^4I_{9/2}$ and $^4F_{5/2} \rightarrow {}^4I_{11/2}$) transitions respectively. Nd-doped materials are primarily used for temperature sensing due to their effectiveness within the first biological window, often employing FIR sensing methods based on Stark sublevel variations for this objective. Therefore, we utilize a FIR approach centered on transitions between Stark sublevels of the $^4F_{3/2}$ level, labeled as FIR (P_2/P_1), observed at 874.8 and 888.5 nm, both falling within the first biological window, characterizing the transitions of ($^4F_{3/2}(P_2)$–$^4I_{9/2}$/$^4F_{3/2}(P_1)$–$^4I_{9/2}$). Fig. 10(a–c) displays the outcomes of the FIR (P_3/P_1) and FIR (P_2/P_1) signal on a semi-ln scale plotted against the inverse of the temperature using equation (1). The Ln (FIR) curves exhibit almost linear trends concerning temperature, aligning with the thermal coupling theory involving the previously discussed excited levels E1 and E2 in Section 2.3. The experimental data of the presented FIR were effectively fitted, yielding a value of energy variance between the thermalized excited states of $\Delta E = 67.75\ cm^{-1}$, obtained for the FIR P2/P1 and for the ratio P3/P1, the energy gap was much higher to be around 744.01 cm^{-1}.The large value of the energy gaps obtained from the FIR P3/P1 curve suggests that large sensitivity can be achieved using this temperature dependent intensity ratio.

The performance of these FIR sensor strategies was assessed by computing their absolute and relative sensitivities to temperature alterations. The *Sa* and *Sr* values derived from equations (2) and (3) are graphically depicted in Fig. 10(b–d). It is noticeable that while both *Sr* and *Sa* values steadily decline as temperature increases, the *Sa* for FIR (P_3/P_1) shows an opposing trend by rising with higher temperatures. In evaluating temperature sensor performance, the relative sensitivity derived from FIR has been identified as crucial, enabling a direct comparison between various sensing methods. An examination of the relative sensitivity in FIR (P_3/P_1) scheme based on the thermal coupling ($^4F_{3/2} \rightarrow {}^4I_{9/2}$ and $^4F_{5/2} \rightarrow {}^4I_{11/2}$) revealed that this strategy exhibited the paramount results, showing high relative sensitivity (*Sr*) value to temperature variations, reaching up to 1.16 $\%K^{-1}$ at 303 K. However, sensors based on Stark sublevels ($^4F_{3/2} \rightarrow {}^4I_{9/2}$) exhibited diminished relative sensitivity values within the physiological range reaching maxima of $Sr = 0.10\ \%K^{-1}$ at 303 K. This can be attributed to the energy gap existing between the pair of levels utilized in the FIR calculations. Indeed, given that the energy difference between the $^4F_{3/2}$ Stark sublevels is less than the energy gaps between the $^4F_{5/2}$ and $^4F_{3/2}$ levels, the sensor's relative sensitivity using the Stark sublevel pair is inferior to the sensitivities acquired from the alternative level pair. Table 2 compares the peak relative sensitivity (*Sr*) values of the methods used in $Sr_6Y_{0.94}(PO_4)_5$:0.06 Nd^{3+} at room temperature, alongside those reported in previous literature.

Here, both the excitation and emission wavelengths reside within the first biological window. Furthermore, the relative and absolute sensitivities achieved are notably elevated when contrasted with other schemes documented in the literature.

The temperature uncertainty, determined through equation (4) as mentioned earlier, is depicted in Fig. 11 (a). Within the temperature range of 303–473 K, δT ranges from 0.131 to 0.310 K, with $\Delta FIR/FIR$ approximately at 1.4 %, derived from the standard deviation of multiple luminescence spectra. To assess the repeatability of the thermometric correlation, the luminescence intensity ratio P_2/P_1 was analyzed for the 6 mol% Nd^{3+} sample, with spectra collected during both heating (473 K) and cooling (303 K) cycles. As illustrated in Fig. 11 (b), at 303 K, a temperature measurement reproducibility of over 94.45 % was observed, with the maximum variation identified as only 5.55 %. The

Table 2
Comparison of relative sensitivities for different Nd^{3+}- doped host materials.

Host material	λ_{ex} (nm)	FIR (emitting levels)	Temperature range (K)	Sr (%K^{-1})	Ref.
$LiBaPO_4$	808	$^4F_{5/2}$-$^4I_{11/2}$/$^4F_{3/2}$-$^4I_{9/2}$	294–423	1.14	[64]
		$^4F_{3/2}$ (2)/$^4F_{3/2}$ (1)		0.097	
	532	$^4F_{5/2}$-$^4I_{11/2}$/$^4F_{3/2}$-$^4I_{9/2}$		0.97	
		$^4F_{3/2}$ (2)/$^4F_{3/2}$ (1)		0.085	
YAG	808	$^4F_{3/2}$(R_2, R_1)-$^4I_{9/2}$ (Z_5)	283–343	0.15	[65]
$LiLaP_4O_{12}$	830	$^4F_{3/2}$(R_2, R_1)-$^4I_{9/2}$ (Z_5)	83–600	0.31	[66]
$KLaP_4O_{12}$				0.0976	
$NaLaP_4O_{12}$				0.1043	
$RbLaP_4O_{12}$				0.1080	
$KGd(WO_4)_2$	808	$^4F_{3/2}$-$^4I_{9/2}$	298–333	0.12	[67]
Bi_2SiO	808	$^4F_{3/}$ -$^4I_{9/2}$	293–338	0.34	[30]
$Sr_6Y(PO_4)_5$	808	$^4F_{5/2}$-$^4I_{11/2}$/$^4F_{3/2}$-$^4I_{9/2}$	303–473	1.16	This work
		$^4F_{3/2}$-$^4I_{9/2}$	303–473	0.10	

FIR P3/P1 also exhibited the same degree of variation. In conventional detection systems, it is generally required to have a temperature uncertainty of less than 0.5 K ($\delta T < 0.5$ K) at 300 K [68] for portable detectors. Hence, the phosphor $Sr_6Y(PO_4)_5$: Nd^{3+} emerges as a promising choice for creating temperature sensors that are both more effective and economical, suitable for various applications.

4. Conclusion

In a conclusory step, a recently developed phosphor, $Sr_6Y_{1-x}(PO_4)_5$: xNd^{3+}, which emits near infrared light, was efficiently synthesized via a high-temperature solid-state reaction. X-ray diffraction (XRD) analysis verified its monoclinic phase, belonging to the whitlockite structural type within space group *I2/a*. Next, it was characterized by photoluminescence spectroscopy at an excitation wavelength of 800 nm, with the aim of using this material for optical temperature detection. This phosphor displayed near-infrared emission bands associated with transitions from $^4F_{3/2}$ to $^4I_{9/2}$ (874.8 nm), $^4F_{5/2}$ to $^4I_{11/2}$ (956 nm), $^4F_{3/2}$ to $^4I_{11/2}$ (1058 nm) and $^4F_{3/2}$ to $^4I_{13/2}$ (1330 nm). The critical concentration for quenching in $Sr_6Y(PO_4)_5$: Nd^{3+} was found to be 0.06 mol, indicating the highest emission intensity. Dipole-dipole (d-d) interaction was identified as a significant contributor to the quenching mechanism. The efficacy of these powdered crystals in functioning as luminescent thermometers was assessed across temperatures ranging from 303 to 473 K. This study delved into exploring different strategies for sensing applications using FIR technology, specifically focusing on Stark sublevels ($^4F_{3/2}$) and transitions occurring between ($^4F_{3/2}$ to $^4I_{9/2}$) and ($^4F_{5/2}$ to $^4I_{11/2}$) energy states. The research revealed that among various FIR methods using infrared excitation, the approach associated with the thermal coupling of energy levels ($^4F_{5/2} \rightarrow {}^4I_{11/2}$) and ($^4F_{3/2} \rightarrow {}^4I_{9/2}$) exhibited superior performance compared to other techniques, demonstrating the highest relative sensitivity of 1.16 $\%K^{-1}$ at 303 K. These results indicate that SYP: Nd^{3+} particles might be highly useful for accurately sensing temperature in a range of biological and technical applications.

Funding

This research article has been possible with the support of the Secretaria d'Universitas i Recerca del Departament d'Empresa i Coneixement de la Generalitat de Catalunya, the European Union (UE), and the European Social Fund (ESF) (2021 FI_B1 00170). Grant PID2022-141499OB-I00 funded by MCIN/AEI/10.13039/501100011033.

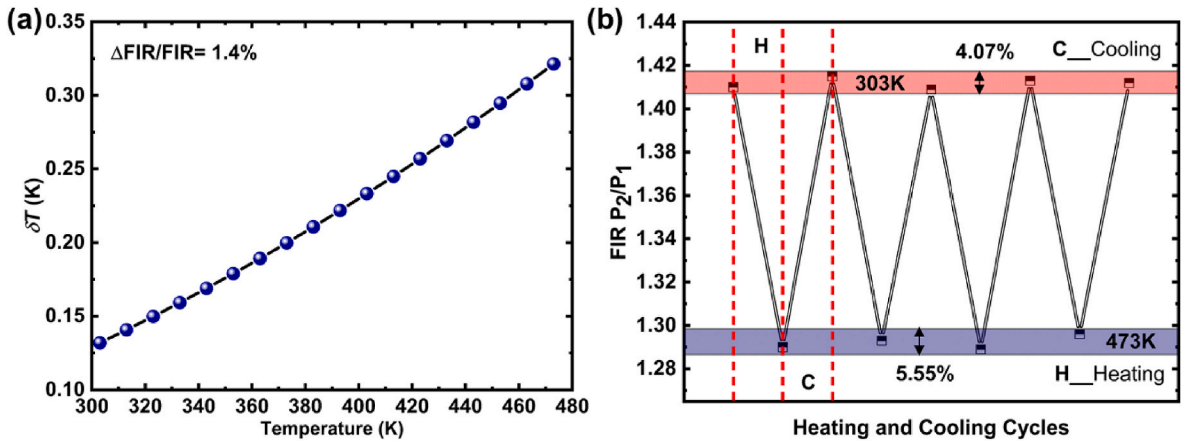

Fig. 11. **(a)** Variation of temperature uncertainty (δT) as a function of temperature (303–473 K). **(b)** Repeatability of $Sr_6Y(PO_4)_5$ doped 6 mol% Nd^{3+} sample for temperature cycling of FIR- The spectra were collected in heating (473 K) and cooling (303 K) cycles.

Declaration of interest statement

The authors declare that they have no conflict of interest exists, or if such conflict exists, the exact nature of the conflict must be declared and if accepted, the article will not be published elsewhere in the same form, in any language, without the written consent of the publisher.

CRediT authorship contribution statement

Ines Mokni: Investigation, Methodology, Writing – original draft. **Sami Slimi:** Investigation, Methodology, Writing – original draft. **Abdessalem Badri:** Conceptualization, Funding acquisition, Supervision, Writing – review & editing. **Rosa Maria Solé:** Investigation, Supervision. **Magdalena Aguiló:** Data curation, Investigation, Writing – review & editing. **Francesc Díaz:** Funding acquisition, Project administration, Writing – review & editing. **Brahim Ayed:** Investigation, Supervision, Writing – review & editing. **Xavier Mateos:** Conceptualization, Funding acquisition, Project administration, Supervision, Writing – review & editing.

Acknowledgements

The authors are grateful to the DGRS (Direction Générale de la Recherche Scientifique) of the Tunisian Ministry of Higher Education and Scientific Research for financial support.

References

[1] C.H. Huang, T.M. Chen, Novel yellow-emitting $Sr_8MgLn(PO_4)_7$: Eu^{2+} (Ln= Y, La) phosphors for applications in white LEDs with excellent color rendering index, Inorg. Chem. 50 (2011) 5725–5730.
[2] D. Wen, Z. Dong, J. Shi, M. Gong, M. Wu, Standard white-emitting $Ca_8MgY(PO_4)_7$: Eu^{2+}, Mn^{2+} phosphor for white-light-emitting LEDs, ECS J. Solid State Sci. Technol. 2 (2013) R178.
[3] S. Lakshmanaperumal, C. Mahendran, Structural, dielectric, cytocompatibility, and in vitro bioactivity studies of yttrium and strontium co-substituted nano-hydroxyapatite by sol–gel method, J. Sol. Gel Sci. Technol. 88 (2018) 296–308.
[4] M. Huchede, T.T.N. Nguyen, L. Cardenas, M. Aouine, K. Jaillardon, J.M.M. Millet, Structure sensitivity of 2,3-butanediol dehydration to butadiene over rare earth orthophosphate catalysts, J. Phys. Chem. 124 (2019) 2060–2069.
[5] G.D. Wu, X.Q. Yin, M.D. Fan, F.P. Yu, S.Z. Fan, Z.P. Wang, X. Zhao, Nd-doped structurally disordered $YSr_3(PO_4)_3$ single crystal: growth and laser performances, J. Rare Earths 39 (2021) 1540–1546.
[6] I. Gupta, S. Singh, S. Bhagwan, D. Singh, Rare earth (RE) doped phosphors and their emerging applications: a review, Ceram. Int. 47 (2021) 19282–19303.
[7] V.B. Pawade, A. Zanwar, R.P. Birmod, S.J. Dhoble, L.F. Koao, Optical and bandgap study of rare earth doped phosphate phosphor, J. Mater. Sci. Mater. Electron. 28 (2017) 16306–16313.
[8] K.N. Shinde, S.J. Dhoble, H.C. Swart, K. Park, Phosphate Phosphors for Solid-State Lighting, Springer Science and Business Media, 2012.
[9] Y.K. Su, Y.M. Peng, R.Y. Yang, J.L. Chen, Effects of NaCl flux on microstructure and luminescent characteristics of $KSrPO_4$:Eu^{2+} phosphors, Opt. Mater. 34 (2012) 1598.
[10] Z.C. Wu, J.X. Shi, J. Wang, M.L. Gong, Q. Su, A novel blue-emitting phosphor $LiSrPO_4$: Eu^{2+} for white LEDs, J. Solid State Chem. 179 (2006) 2356–2360.
[11] S. Gai, C. Li, P. Yang, And al, Recent progress in rare earth micro/nanocrystals: soft chemical synthesis, luminescent properties, and biomedical applications, Chem. Rev. 114 (2014) 2343–2389.
[12] X. Wang, Q. Liu, Y. Bu, C.S. Liu, T. Liu, X. Yan, Optical temperature sensing of rare-earth ion doped phosphors, RSC Adv. 5 (2015) 86219–86236.
[13] S.E. Crawford, P.R. Ohodnicki, J.P. Baltrus, Materials for the photoluminescent sensing of rare earth elements: challenges and opportunities, J. Mater. Chem. C 8 (2020) 7975–8006.
[14] Z. Wei, Y. Liu, B. Li, J. Li, S. Lu, X. Xing, H. Zhang, Rare-earth based materials: an effective toolbox for brain imaging, therapy, monitoring and neuromodulation, Light Sci. Appl. 11 (2022) 175.
[15] P.S. Chelushkin, J.R. Shakirova, I.S. Kritchenkov, V.A. Baigildin, S.P. Tunik, Phosphorescent NIR emitters for biomedicine: applications, advances and challenges, Dalton Trans. 51 (2022) 1257–1280.
[17] Grand View Research, Market research report, temperature sensors market analysis by application (automotive, consumer electronics, environmental, medical, process industries) and segment forecasts to. https://www.grandviewresearch.com/industry-analysis/temperature-sensors-marketSanFrancisco2015, 2020. ISBN 978-1-68038-495-6.
[18] C.D. Brites, P.P. Lima, N.J. Silva, A. Millán, V.S. Amaral, F. Palacio, L.D. Carlos, Thermometry at the nanoscale, Nanoscale 4 (2012) 4799–4829.
[19] A.H. Khalid, K. Kontis, Thermographic phosphors for high temperature measurements: principles, current state of the art and recent applications, Sensors 8 (2008) 5673–5744.
[20] F. Chi, B. Jiang, Z. Zhao, Y. Chen, X. Wei, C. Duan, M. Yin, W. Xu, Multimodal temperature sensing using Zn_2GeO_4:Mn^{2+} phosphor as highly sensitive luminescent thermometer, Sensor. Actuator. B Chem. 296 (2019) 126640.
[21] D.K. Amarasinghe, F.A. Rabuffetti, Bandshift luminescence thermometry using Mn^{4+}:$Na_4Mg(WO_4)_3$ phosphors, Chem. Mater. 31 (2019) 10197e10204.
[22] Y. Tian, Y. Tian, P. Huang, L. Wang, Q. Shi, C. Cui, Effect of Yb^{3+} concentration on upconversion luminescence and temperature sensing behavior in Yb^{3+}/Er^{3+} co-doped $YNbO_4$ nanoparticles prepared via molten salt route, Chem. Eng. J. 297 (2016) 26–34.
[23] Q. Wang, Z. Mu, S. Zhang, Q. Du, Y. Qian, D. Zhu, F. Wu, Bi^{3+} and Sm^{3+} codoped La_2MgGeO_6: a novel color-temperature indicator based on different heat quenching behavior from different luminescent centers, J. Lumin. 206 (2019) 462–468.
[24] M.A. Hernandez-Rodríguez, A.D. Lozano-Gorrín, I.R. Martín, U.R. Rodríguez-Mendoza, V. Lavín, Comparison of the sensitivity as optical temperature sensor of nano perovskite doped with Nd^{3+} ions in the first and second biological windows, Sensor. Actuator. B Chem. 255 (2018) 970–976.
[25] Z. Zhao, F. Hu, Z. Cao, F. Chi, X. Wei, Y. Chen, C. Duan, M. Yin, Highly uniform and monodisperse b-$NaYF_4$:Sm^{3+} nanoparticles for a nanoscale optical thermometer, Opt. Lett. 43 (2018) 835–838.
[26] S.A. Wade, J.C. Muscat, S.F. Collins, G.W. Baxter, Nd^{3+}-doped optical fiber temperature sensor using the fluorescence intensity ratio technique, Rev. Sci. Instrum. 70 (1999) 4279–4282.
[27] Q. Wang, M. Liao, Q. Lin, M. Xiong, Z. Mu, F. Wu, A review on fluorescence intensity ratio thermometer based on rare-earth and transition metal ions doped inorganic luminescent materials, J. Alloys Compd. 850 (2021) 156744.
[28] X. Li, R. Wang, F. Zhang, L. Zhou, D. Shen, C. Yao, D. Zhao, Nd^{3+} sensitized up/down converting dual-mode nanomaterials for efficient in-vitro and in-vivo bioimaging excited at 800 nm, Sci. Rep. 3 (2013) 3536.
[29] P.P. Sukul, K. Kumar, Near-infrared (808 and 980 nm) excited photoluminescence study in Nd-doped Y_2O_3 phosphor for bio-imaging, Methods Appl. Fluoresc. 4 (2016) 044005.

[30] D. Chen, Y. Liang, S. Miao, J. Bi, K. Sun, Nd^{3+}-doped Bi_2SiO_5 nanospheres for stable ratiometric optical thermometry in the first biological window, J. Lumin. 234 (2021) 117967.

[31] B. Zheng, J. Fan, B. Chen, X. Qin, J. Wang, F. Wang, X. Liu, Rare-earth doping in nanostructured inorganic materials, Chem. Rev. 122 (2022) 5519–5603.

[32] M.T. Abbas, N.Z. Khan, J. Mao, L. Qiu, X. Wei, Y. Chen, S.A. Khan, Lanthanide and transition metals doped materials for non-contact optical thermometry with promising approaches, Mater. Today Chem. 24 (2022) 100903.

[33] M.D. Dramićanin, Trends in luminescence thermometry, J. Appl. Phys. 128 (2020) 040902.

[34] D. Wawrzynczyk, A. Bednarkiewicz, M. Nyk, W. Strek, M. Samoc, Neodymium (III) doped fluoride nanoparticles as non-contact optical temperature sensors, Nanoscale 4 (2012) 6959–6961.

[35] A.A. Belik, F. Izumi, T. Ikeda, M. Okui, A.P. Malakho, V.A. Morozov, B.I. Lazoryak, Whitlockite-related phosphates $Sr_9A(PO_4)_7$ (A= Sc, Cr, Fe, Ga, and In): structure refinement of $Sr_9In(PO_4)_7$ with synchrotron X-ray powder diffraction data, J. Solid State Chem. 168 (2002) 237–244.

[36] J. Faber, T. Fawcett, The powder diffraction file: present and future, Acta Crystallogr. B 58 (3) (2002) 325–332.

[37] M. Chowdhury, S.K. Sharma, Spectroscopic behavior of Eu^{3+} in SnO_2 for tunable red emission in solid-state lighting devices, RSC Adv. 5 (2015) 51102.

[38] V.P.R. Hedaoo, V.B. Bhatkar, S.K. Omanwar, Combustion synthesis and photoluminescence in novel red emitting yttrium gadolinium pyrosilicate nanocrystalline phosphor, J. Alloys Compd. 672 (2016) 653–659.

[39] Robert D. Shannon, Revised effective ionic radii and systematic studies of interatomic distances in halides and chalcogenides, Acta Crystallogr. Sect. A Cryst. Phys. Diffr. Theor. Gen. Crystallogr. 32 (1976) 751–767.

[40] A. Taylor, H. Sinclair, On the determination of lattice parameters by the Debye-Scherrer method, Proc. Phys. Soc. 57 (1945) 126.

[41] A. Badri, M. Jabli, A. Wattiaux, M.B. Amara, Crystal structure, Mössbauer spectroscopy and dye adsorption properties of a new layered iron phosphate $RbMgFe(PO_4)_2$, J. Mol. Struct. 1167 (2018) 161–168.

[42] I. Mokni, A. Badri, S. Slimi, K. Omri, P. Loiko, R.M. Solé, M.B. Amara, Synthesis and characterization of a novel alkali mixed magnesium-aluminum phosphate with a layeredstructure–$KMgAl(PO_4)_2$, J. Mol. Struct. 1248 (2022) 131535.

[43] L.C. Kravitz, J.D. Kingsley, E.L. Elkin, Raman and infrared studies of coupled PO_4^{3-}vibrations, J. Chem. Phys. 49 (1968) 4600–4610.

[44] S.A. Kovyazina, L.A. Perelyaeva, O.N. Leonidova, I.A. Leonidov, A.L. Ivanovskii, High-temperature Raman spectroscopy and phase transformations in phosphates and vanadates $Ca_{3-3x}Nd_{2x}(AO_4)_2$ (A= P, V; 0≤ x≤ 0.14), Crystallogr. Rep. 49 (2004) 211–214.

[45] S.N. Britvin, M.G. Krzhizhanovskaya, V.N. Bocharov, E.V. Obolonskaya, Crystal chemistry of stanfieldite, $Ca_7M_2Mg_9(PO_4)_{12}$ (M= Ca, Mg, Fe^{2+}), a structural base of $Ca_3Mg_3(PO_4)_4$ phosphors, Crystals 10 (2020) 464.

[46] M.J. Bushiri, R.S. Jayasree, M. Fakhfakh, V.U. Nayar, Raman and infrared spectral analysis of thallium niobyl phosphates:$Tl_2NbO_2PO_4$, $Tl_3NaNb_4O_9(PO_4)_2$ and $TlNbOP_2O_7$, Mater. Chem. Phys. 73 (2002) 179–185.

[47] X. Hu, L. Liu, S. Zhai, The structure-Raman spectra relationships of $Mg_3(PO_4)_2$ polymorphs: a comprehensive experimental and DFT study Spectrochim, Acta Mol. Biomol. Spectrosc. 245 (2021) 118906.

[48] T. Jenkins, J.A. Alarco, I.D. Mackinnon, Synthesis and characterization of a novel hydrated layered vanadium (III) phosphate phase $K_3V_3(PO_4)_4{\cdot}H_2O$: a functional cathode material for potassium-ion batterieS, ACS Omega 6 (2021) 1917–1929.

[49] P. Sharma, P. Singh, I. Bhushan, K. Pathania, Combustion synthesis of $NaSrVO_4$: Nd^{3+} nanophosphors with enhanced NIR 1.056 μm luminescent performance for solid-state laser and bio-imaging applications, J. Mater. Sci. 57 (2022) 17219–17233.

[50] J. Sun, H. Wang, Y. Zhang, Y. Zheng, Z. Xu, R. Liu, Structure and luminescent properties of electro deposited Eu^{3+}-doped CaF_2 thin films, Thin Solid Films 562 (2014) 478–484.

[51] M. Jiao, C. Yang, M. Liu, Q. Xu, Y. Yu, H. You, Mo^{6+} substitution induced band structure regulation and efficient near-UV-excited red emission in $NaLaMg(W,Mo)O_6$: Eu phosphor, Opt. Mater. Express 7 (2017) 2660–2671.

[52] P. Sharma, P. Singh, Study of synthesis mechanism, structural, optical and luminescent properties of bluish-violet rare earth doped $KSrVO_4$: Nd^{3+} nano powders, Mater. Sci. Eng. B 6 (2022) 115564.

[53] M. Shoaib, G. Rooh, N. Chanthima, H.J. Kim, J. Kaewkhao, Luminescence properties of Nd^{3+} ions doped P_2O_5-Li_2O_3-GdF_3 glasses for laser applications, Optik 199 (2019) 163218.

[54] A.M. Smith, M.C. Mancini, S.M. Nie, Second window for in vivo imaging, Nat. Nanotechnol. 4 (2009) 710.

[55] G. Jiang, X. Wei, S. Zhou, Y. Chen, C. Duan, M. Yin, Neodymium doped lanthanum oxysulfide as optical temperature sensors, J. Lumin. 152 (2014) 156–159.

[56] G.Y. Chen, T.Y. Ohulchanskyy, S. Liu, W.C. Law, F. Wu, M.T. Swihart, P.N. Prasad, Core/shell $NaGdF_4$:Nd^{3+}/$NaGdF_4$ nanocrystals with efficient near-infrared to near-infrared downconversion photoluminescence for bioimaging applications, ACS Nano 6 (2012) 2969–2977.

[57] G.H. Dieke, H.M. Crosswhite, H. Crossawhite, Spectra and Energy Levels of Rare-Earth Ions in Crystals, Wiley, New York, 1968 4826175. NSA-23-005493.

[58] G. Blasse, B.C. Grabmaier, Energy transfer, in: Luminescent Materials, Springer, Berlin, Heidelberg, 1994.

[59] D.L. Dexter, J.H. Schulman, Theory of concentration quenching in inorganic phosphors, J. Chem. Phys. 22 (1954) 1063.

[60] K. Li, M. Dai, Z. Fu, Z. Wang, H. Xu, R. Wang, A latest-generation fluoride with excellent structural stiffness for ultra-efficient photoluminescence and specific four-peak emission temperature sensing, Inorg. Chem. Front. 11 (1) (2024) 172–185.

[61] M. Dai, Z. Fu, Z. Wang, H. Xu, Sc^{3+}-induced double optimization strategies for boosting NIR-II luminescence and improving thermometer performance in CaF2: Nd^{3+}, Nd^{3+}/Yb^{3+}@ $NaYF_4$ nanocrystals, J. Chem. Eng. 452 (2023) 139133.

[62] H. Xu, M. Jia, Z. Wang, Y. Wei, Z. Fu, Enhancing the upconversion luminescence and sensitivity of nanothermometry through advanced design of dumbbell-shaped structured nanoparticles, ACS Appl. Mater. Interfaces 13 (51) (2021) 61506–61517.

[63] F. Auzel, Multiphonon-assisted anti-Stokes and Stokes fluorescence of triply ionized rare-earth ions, Phys. Rev. B 13 (1976) 2809–2817.

[64] A.S. Laia, D.A. Hora, M.V.D.S. Rezende, Y. Xing, J.J. Rodrigues Jr., G.S. Maciel, M. A. Alencar, Nd^{3+}-doped $LiBaPO_4$ phosphors for optical temperature sensing within the first biological window: a new strategy to increase the sensitivity, J. Chem. Eng. 399 (2020) 125742.

[65] A. Benayas, B. Del Rosal, A. Perez-Delgado, K. Santacruz-Gomez, D. Jaque, G. A. Hirata, F. Vetrone, Nd:YAG near-infrared luminescent nanothermometers, Adv. Opt. Mater. 3 (2015) 687–694.

[66] Ł. Marciniak, A. Bednarkiewicz, D. Hreniak, W. Strek, The influence of Nd^{3+} concentration and alkali ions on the sensitivity of non-contact temperature measurements in $ALaP_4O_{12}$:Nd^{3+} (A = Li, K, Na, Rb) nanocrystalline luminescent thermometers, J. Mater. Chem. C 4 (2016) 11284–11290.

[67] O. Savchuk, J.J. Carvajal, L.G. De la Cruz, P. Haro-González, M. Aguiló, F. Díaz, Luminescence thermometry and imaging in the second biological window at high penetration depth with Nd: $KGd(WO_4)_2$ nanoparticles, J. Mater. Chem. C 4 (2016) 7397–7405.

[68] C.D.S. Brites, A. Mill'an, L.D. Carlos, Lanthanides in luminescent thermometry, Chapter 281 -Handb, Phys. Chem. Rare Earths 49 (2016) 339–427.